Density Functional Theory Modeling of the Oxidation Mechanism of Tl(I) by Birnessite

Alain Manceau, Stephan N Steinmann

Density Functional Theory Modeling of the Oxidation Mechanism of Tl(I) by Birnessite

Alain Manceau[*a,b] and Stephan N. Steinmann[a]

[a] ENS de Lyon, CNRS, Laboratoire de Chimie, F-69342 Lyon, France

[b] European Synchrotron Radiation Facility (ESRF), F-38000 Grenoble, France

Corresponding Author :

alain.manceau@ens-lyon.fr

Keywords: Phyllomanganate, thallium, transition state, redox, DFT, hydrolysis

ABSTRACT

This study establishes a theoretical foundation for the oxidation pathway of monovalent thallium (Tl(I)) to trivalent thallium (Tl(III)) on birnessite, which is responsible for the over million times enrichment of Tl in marine ferromanganese deposits over seawater concentration. Tl(I) oxidation occurs on vacant Mn(IV) sites located on basal planes of the birnessite layers and on the edge sites, in agreement with experiment. Two Mn(IV) atoms are reduced to Mn(III) when Tl(I) gives up two electrons in two one-electron steps with formation of an intermediate Tl(II) inner-sphere complex. Tl(I) oxidation is facilitated at pH > 4-5 by the partial hydrolysis of the Tl(III) inner-sphere product on the reactive basal and edge sites. Oxidation by O_2 is thermodynamically unfavorable. Although density functional theory has predictive power for intermediate Tl(II) complex, it would be difficult to characterize as Tl(II) is highly reactive, and therefore probably short-lived. These findings provide the first atomic-scale description of the oxidation of Tl(I) by a manganese oxide and fill gaps in our understanding of global thallium sequestration in natural systems.

1. INTRODUCTION

The oxidative uptake of thallium (Tl) on manganese dioxides (MnO_2) has received much attention over the last few years,[1–16] because of the high toxicity of this element[17–19] and its 10^7 geochemical partitioning between seawater and ferromanganese (FeMn) crust and nodule deposits from the global ocean.[20] Thallium occurs in two oxidation states: monovalent (thallous cation; Tl(I)) and trivalent (thallic cation; Tl(III)). Ionic Tl^+ is the predominant Tl(I) species in aquatic environment,[21] for its

complexes with carbonate, sulfate, phosphate, and chloride anions are weak and its hydrolysis insignificant.[22] Tl(I) chemistry resembles that of the alkali metals, and in soils it substitutes for K^+ in clay minerals.[11,9,12] Tl(III) undergoes extensive hydrolysis and is oxidatively scavenged by MnO_2 minerals of the birnessite group.[1–3,5–8,23]

Birnessites are non-stoichiometric phyllomanganates with general formula $(Mn^{4+}_x Mn^{3+}_y \square_z)O_{2-y/2-2z}$, where □ represents a Mn(IV) vacancy.[24–28] Laboratory experiments conducted at pH 4-8 on synthetic birnessite showed that Tl(I) is oxidized on both the layer vacancy and edge sites as long as the Mn(III) content of the sorbent is low.[1–4] Layer vacancies are bordered on each side of the MnO_2 layer by three doubly-coordinated oxygen atoms (O_{2Mn}), and the +4 charge deficit resulting from the missing Mn^{4+} cation is balanced at acidic pH by four protons, two above and two below the vacancy (OH_{2Mn} groups, Figure 1a).[25] Tl(III) bonds to the three surface O_{2Mn} atoms, forming a triple-corner-sharing (TCS) complex, and its six-fold coordination is completed with three water molecules ($Tl^{3+}_{3W,3O}$, Figure 1b).[2,8] The protons from the two OH_{2Mn} hydroxyl groups are released to solution, and therefore Tl(I) oxidation is pH-dependent and favored at circumneutral pH. Tl(III) is considered to bond the layer edges through the sharing of two edges from two adjacent MnO_6 octahedra, forming a double-edge-sharing (DES) complex.[2,8] The Tl(III) octahedra are attached to the lateral surfaces via three surface oxygens, and therefore their coordination is also completed with three water molecules, like the TCS complex. Under this scheme, Tl(III) sorption on layer edges releases the OH_{2Mn} proton shared by the two surface MnO_6 octahedra ($Tl^{3+}_{3W,2OH,O}$, Figure 1c).

The TCS and DES complexes have been observed in 2022 on marine FeMn deposits using X-ray absorption spectroscopy (XANES and EXAFS).[8] The thallium atoms were not all oxidized, however, with up to 38% of them being Tl(I) in FeMn crusts. The proportion of Tl(I) reached 58 ± 3% in an earlier 2012 study by Peacock and Moon,[1] also on FeMn crusts. K and Ba sorb with high affinity above the tetrahedral cavities of the MnO_2 layer,[29–32] and the FeMn crusts from the 2022 study contained as much as 1523 ± 558 mg/kg (ppm) Ba, compared to a Tl concentration between 1.5 mg/kg (ppm) and 319 mg/kg. For these reasons, Tl(I) was assumed to occupy the Ba site on MnO_2 layers that did not have vacancies and on layers which had their vacancies capped with another cation, thus preventing Tl(I) from being oxidized on basal surfaces.[8] The second scenario is supported experimentally by the observation of Wick et al.[2] that the oxidative uptake of Tl(I) on nanoparticulate birnessite (δ-MnO_2)[28] is constrained by the availability of unblocked vacant sites. Tl(I) does not appear to be able to displace interlayer Mn(III) complexed on the layer vacancies of birnessite, in contrast to

Co(II).[33–35] A likely reason is the weak acidity of Tl(I) with an hydrolysis constant of pK_a = 11.7.[36] This, in turn, helps to explain the high stability of Tl(I) in surficial environments and its co-occurrence with Tl(III) on birnessite, despite the high oxidative properties of Mn(III) and Mn(IV).

Here, we use density functional theory (DFT) to gain atomic level insight into the molecular mechanism of the Tl(I) → Tl(III) oxidation on the vacant layer sites and edge sites of birnessite. The computational approach follows the modeling scheme used previously for the Co(II) → Co(III) oxidation.[33] The thermodynamic feasibility of a number of reaction pathways is evaluated from the calculation of the Gibbs free energies (ΔG) of complexation and oxidation of Tl(I) on vacancy-containing and vacancy-free MnO_2 nanolayers. In contrast to Co, the oxidative uptake of Tl involves the transfer of two electrons to manganese, and therefore the question arises whether the oxidation occurs via two one-electron transfer steps or via a single two-electron transfer step. The first scenario requires the stabilization of an intermediate Tl(II) complex.

This study is divided in three parts. The first part focuses on the molecular structure of aqueous Tl(I) that will be used in the modeling of the birnessite surface reactions. The second and third parts deal with the complexation and oxidation of Tl(I) on vacant nanolayer sites and edge sites, respectively. These two parts are each divided in two sections, with the first presenting the construction of the vacancy-containing and vacancy-free MnO_2 layers, and the second providing the ΔG of complexation and oxidation of the reaction pathways.

2. COMPUTATIONAL DETAILS

Spin-unrestricted DFT calculations were performed on cluster models with ORCA 5.0.3[37] and a computational methodology similar to that used previously to study the complexation energetics of Co(II)/Co(III), Ni(II), Cu(II), Zn(II), and Pb(II) on birnessite.[33,38] In ref 33, we investigated the effect of the size of the birnessite model on DFT results. Using protons to yield (nearly) charge-neutral, symmetric systems, we found that a cluster model with 18 Mn(IV) octahedra provides robust results. Still, instead of protons, it is possible to embed the cluster in a distribution of point-charges that would reproduce the Madelung potential corresponding to a periodic system.[39] However, to study the reactivity of birnessite, and in particular to compare the reactivity of the edge and basal-plane sites, the use of protons is more suitable. The hybrid PBE0[40,41] functional of the generalized gradient approximation (GGA) was used to describe the exchange-correlation function together with the atom-pairwise dispersion correction D3BJ.[42] The electronic configurations of all atoms, except Tl, were treated with the all-electron polarized def2-TZVP basis sets of triple ζ quality.[43] Scalar relativistic

effects of Tl were accounted for using the effective core potential (ECP) parameters of Metz et al..[44] The Coulomb fitting auxiliary def2/J basis sets were used to accelerate calculations.[45] Frequency calculations were carried out at 1 atm and 298.15 K on cluster models geometrically optimized with a convergence criterium of 10^{-8} Eh between two SCF cycles (TightSCF).

The total entropy of the reactant and product birnessite models was obtained by summing the electronic and vibrational entropies and omitting the rotational and translational entropies, which do not exist in a solid as atoms are held together.[46] The water solvent was modeled with the continuum solvent model SMD,[47] and all energies reported are free energies in solution (i.e., sometimes denoted as ΔG^*) and in kcal/mol. The proton solvation energy was taken to be −264.0 kcal/mol.[48] The energetics of the Tl(I) → Tl(III) electron transfer was modeled using the minimum energy crossing point (MECP) procedure proposed by Harvey et al.[49], as implemented with the SurfCrossOpt keyword in ORCA.

The accuracy of prediction of ΔG obtained with the afore described computational methodology has been benchmarked previously[33,38] with the first hydrolysis constants of the hexahydrated Mn^{2+}, Co^{2+}, Ni^{2+}, and Zn^{2+} ions.[50] ΔG values for these ions are calculated reliably within chemical accuracy (1−2 kcal/mol). The method accuracy was further validated here with Tl^{+}: pK_a(exp) = 13.2 ± 1,[50] corresponding to ΔG = 18.0 kcal/mol, and pK_a(calc.) = 16.5, corresponding to ΔG = 22.5 kcal/mol. Therefore, the computational procedure probably tends to overestimate ΔG values by approximately 4.5 kcal/mol. The total electronic charges of the cluster models, and their Mulliken atomic spin densities and multiplicities are listed in Table S1.

3. RESULTS AND DISCUSSION

3.1. Structure of Solvated Tl(I). The first coordination sphere of the Tl(I) ion in aqueous solution was characterized by Persson et al.[51] using large-angle X-ray scattering and EXAFS spectroscopy. Tl(I) has two nearest bonds at about 2.73(1) Å to water molecules ($Tl(H_2O)_2$). The DFT Tl-O distances are 2.89 Å and 3.02 Å. The predicted bond lengthening compared to experiment was confirmed by increasing the level of theory to the second-order Møller−Plesset perturbation theory (MP2, 2.95 Å and 3.05 Å). The DFT and MP2 O-Tl-O angles are the same (55.8(2)°) (Figure 2a). The difference of bond length between experiment and prediction comes from the weak electrostatic interactions and covalent contribution of Tl(I) with its ligands. Tl(I) has a formal $5d^{10}6s^2$ valence shell with a stereochemically active $6s^2$ lone electron pair.[51] The electron configuration of Tl(I) calculated by natural population analysis (NPA)[52] of the DFT $[Tl(H_2O)_2]^{1+}$ ion is $5d^{10}6s^26p^{0.02}$. Thus, monovalent

Tl has a natural charge of 0.98, consistent with its weak bonding character and solvated coordination. The stereochemical activity of the $6s^2$ lone pair was confirmed in this study with a natural bond orbital (NBO)[53,54] analysis of the electronic structure of the DFT model.

3.2. Tl(I) Oxidation on Vacant Layer Sites. *3.2.1. Cluster model.* The MnO_2 nanolayer used to model the oxidation of Tl(I) on vacancies counts 18 Mn(IV) octahedra and has an empty octahedron at the center ($Mn_{18}^{4+}V$, Figure 2a). This size was large enough to prevent the water molecules reacting with Tl from being attracted to the edge sites. One water molecule was added on the basal surface to complete to six the coordination of Tl(III) in TCS position as aqueous Tl(I) is coordinated to only two H_2O ($Mn_{18}^{4+}VW$, Figure 1b). The added H_2O is hydrogen bonded to a OH_{2Mn} and a O_{3Mn} oxygen near the vacancy in the $Mn_{18}^{4+}VW$ model of Figure 2a. Placing the H_2O above other oxygen atoms of the MnO_2 nanolayer marginally changed the Gibbs free energies of the oxidation-reduction reactions. The composition of $Mn_{18}^{4+}VW$ is $Mn_{18}O_{55}H_{36}$, its electronic charge is -2, and its spin multiplicity is M = 2S + 1 = 55, where S is the total spin angular momentum of the system.

3.2.2. Energetics of the $Tl(H_2O)_2$ Adsorption. The sorption of $Tl(H_2O)_2$ close to the two OH_{2Mn} groups of a vacancy is thermodynamically favorable with ΔG = -5.1 kcal/mol (reaction 1, Figure 2a). The two coordinated H_2O are at 2.74 Å and 2.79 Å from Tl(I) and the nearest surface oxygen (O_{2Mn}) is at 2.78 Å. The third H_2O is at 3.89 Å. The $Tl_{2W,O}^{1+}$ complex is unstable, however, as Tl(I) prefers to form a dehydrated Tl_{3O}^{1+} three-fold complex above the layer vacancy (reaction 2, Figure 2b). The three O_{2Mn} oxygen atoms are at 2.68-2.73 Å, and the three oxygen atoms from the water molecules are at 3.33 Å, 3.65 Å, and 3.68 Å, from Tl(I). A three-fold Tl(I) coordination is unstable in solution, unless it is stabilized by three H-bonds with a fourth water molecule (Figure S1). On a vacancy site, the three-fold Tl_{3O}^{1+} configuration is stabilized by the three Tl(I)-O_{2Mn} bonds.

Reaction 2 has ΔG = 3.5 kcal/mol, that is around 0.0 kcal/mol after correction of the ~4.5 kcal/mol overestimation of the DFT calculation (section 2). The two protons from the OH_{2Mn} groups are released when Tl(I) sits over a vacant Mn site, which drives the reaction forward. Its equilibrium constant (K_{eq}) can be calculated from the Gibbs free energy (G) change of the reactants and products according to $\ln K_{eq} = -\Delta G/RT$. This constant allows calculation of the equilibrium ratio of the $Tl_{2W,O}^{1+}$ and Tl_{3O}^{1+} complexes at given pH according to $Tl_{3O}^{1+}/[Tl_{2W,O}^{1+}] = K_{eq}/[H^+]^2$. Taking ΔG = 3.5 kcal/mol yields $[Tl_{3O}^{1+}]/[Tl_{2W,O}^{1+}] = 3.0 \times 10^7$ at pH 5 and 2.7×10^{11} at pH 7, showing that Tl(I) sorption in TCS position is thermodynamically favorable. Still, the affinity of solvated Tl(I) for this site is low

(ΔG(reactions 1+2) = -5.1 + 3.5 = -1.6 kcal/mol) in comparison to those of the aqua $[Ni(H_2O)_6]^{2+}$ (-11.6 kcal/mol), $[Cu(H_2O)_6]^{2+}$ (-20.5 kcal/mol), and $[Zn(H_2O)_6]^{2+}$ (-10.8 kcal/mol) species.[33] Thus, Tl(I) does not outcompete transition metals and appears to sorb only on unoccupied TCS sites, in agreement with Wick et al.'s[2] suggestion.

3.2.3. The Tl(I)-Mn(IV) Oxidation Pathway. Tl(I) is likely oxidized to Tl(III) by Mn(IV), because laboratory experiments show that oxidative uptake of Tl(I) is inhibited on Mn(III)-rich δ-MnO_2.[2] Oxidation by dissolved oxygen cannot be excluded, however, as no precaution was taken to exclude O_2 in previous experiments.[1–4] Tl oxidation by the donation of two electrons (Tl(I) → Tl(III)) to molecular oxygen will be described after the Mn(IV) pathway.

According to EXAFS spectroscopy, Tl is 3+ and octahedrally coordinated over layer vacancies.[2,8] When the three water molecules at 3.33 Å, 3.65 Å, and 3.68 Å from Tl(I) in the Tl^{1+}_{3O} complex are bonded to Tl to complete its coordination to six and the spin multiplicity of the complex unchanged (M = 55), the Mulliken atomic spin density of Tl decreases from 0.01 ($5d^{10}6s^2$ valence shell) to -0.60 ($5d^{10}6s^1$ valence shell) and the spin density of a nearest Mn atom increases from 3.12 ($3d^34s^2$ valence shell) to 3.97 ($3d^44s^2$ valence shell). Tl is now 2+ and its oxidation is accompanied by the reduction of one Mn(IV) to Mn(III) (reaction 3, Figure 2c). The $Tl^{2+}_{3W,3O}$ complex is a stable intermediate state, in which Tl(II) is antiferromagnetically coupled to Mn(III). The new $Tl^{2+}_{3W,3O}$ complex is ΔG = 19.5 kcal/mol higher in energy than the Tl^{1+}_{3O} reactant. When the multiplicity is 57, Tl is ferromagnetically coupled to Mn(III) (spin density 0.62) and the new complex is 2 kcal/mol higher in energy than the antiferromagnetic complex. The three water molecules of $Tl^{2+}_{3W,3O}$ are at 2.62-2.65 Å from Tl and the three O_{2Mn} are at 2.33-2.39 Å. Tl(II) may also form a four-fold $Tl^{2+}_{W,3O}$, and a five-fold $Tl^{2+}_{2W,3O}$, complex above a vacancy site (Figure S2). Their formation is, however, energetically less favorable than that of the $Tl^{2+}_{3W,3O}$ complex (ΔG = 24.6 and 23.9 kcal/mol, respectively).

When the Tl-H_2O bond distances of $Tl^{2+}_{3W,3O}$ are reduced to about 2.4 Å and the Tl-O_{2Mn} to about 2.2 Å, to approach the EXAFS values of the Tl(III)-TCS complex,[8] and $Tl^{2+}_{3W,3O}$ geometrically reoptimized with M = 57, the lowest energy structure is 17 kcal/mol more stable, d(Tl-H_2O) = 2.30-2.33 Å and d(O_{2Mn}) = 2.16-2.20 Å, Tl has a spin density of 0.03 ($5d^{10}6s^0$ valence shell) and two Mn atoms have a spin density of 3.97-4.01. Tl(II) is therefore oxidized to Tl(III) by a second Mn(IV)

(reaction 4, Figure 2d). Formation of the $Tl^{3+}_{3W,3O}$ complex from Tl^{1+}_{3O} is predicted to be endergonic since ΔG(reactions 3+4) = 2.3 kcal/mol.

However, recalling that Tl(III) is highly hydrolyzable, $Tl^{3+}_{3W,3O}$ may be further stabilized by deprotonation. This hypothesis was tested by calculating the acid dissociation constants of the three water molecules

$$Tl^{3+}_{3W,3O} \rightarrow Tl^{3+}_{2W,OH,3O} + H^+, \Delta G = 10.2 \text{ kcal/mol}, pK_1 = 7.5 \text{ (reaction 5)}$$

$$Tl^{3+}_{2W,OH,3O} \rightarrow Tl^{3+}_{1W,2OH,3O} + H^+, \Delta G = 19.9 \text{ kcal/mol}, pK_2 = 14.6 \text{ (reaction 6)}$$

$$Tl^{3+}_{1W,2OH,3O} \rightarrow Tl^{3+}_{3OH,3O} + H^+, \Delta G = 24.3 \text{ kcal/mol}, pK_3 = 17.8 \text{ (reaction 7)}$$

The release of one proton drives reaction 5 forward (i.e, [Product]>[Reactant]) at pH > 7.5, despite the positive value of ΔG, and therefore stabilizes $Tl^{3+}_{2W,OH,3O}$ relative to $Tl^{3+}_{3W,3O}$. The three predicted hydrolysis constants can be safely corrected for the 4.5 kcal/mol ΔG overestimate of the DFT calculation (section 2), as this value was obtained by benchmarking the predicted hydrolysis constant of aqueous Tl(I) with experiment. Subtracting 4.5 kcal/mol to ΔG = 10.2 kcal/mol yields ΔG = 5.7 kcal/mol and pK_1 = 4.2 for reaction 5. After correction, the second deprotonation occurs at pH > 11.3. We conclude that $Tl^{3+}_{2W,OH,3O}$ prevails on basal surfaces at pH > 4.2, and that the oxidation pathway of Tl(I) to Tl(III) described in Figure 2 is thermodynamically favorable.

Existence of the $Tl^{2+}_{3W,3O}$ intermediate means that the oxidation-reduction reaction takes place in two successive one-electron steps rather than by a single step in which two electrons are transferred at once. The two transition states (TS1 and TS2), in which the electrons are transferred from Tl to Mn were located using the nudge elastic band optimizer (NEB)[55] method implemented into ORCA. The NEB-optimized energy profiles for the $Tl^{1+}_{3O} \rightarrow Tl^{2+}_{3W,3O}$ and $Tl^{2+}_{3W,3O} \rightarrow Tl^{3+}_{3W,3O}$ reaction paths are shown in Figure 3. The two activation barriers are 3-4 kcal/mol high. A frequency analysis was performed subsequently on the two high energy structures to identify the vibrational modes of TS1 and TS2. Two vibrational modes were obtained for TS1 of imaginary frequencies ω_1 = -78 cm^{-1} and ω_2 = -65 cm^{-1}. Technically, a TS must contain a single imaginary frequency that pertains to the bond breaking/forming in the molecular system. Attempts to obtain a single negative frequency by re-optimizing the TS geometry with the calculation of the full Hessian matrix failed due to the high numerical cost of the calculation. The two imaginary frequencies are small in absolute value, which means, on one hand, that numerical noise makes it challenging to obtain a single frequency and, on

the other hand, that the energetic impact of the double negative frequency should be negligible. The ω_1 frequency is a conformational TS, in which the unbound H_2O molecule rotates in direction of a O_{3Mn} surface oxygen to create a H-bond (Video S1). The ω_2 frequency is the reaction path TS and corresponds to the formation of the three Tl-H_2O bonds (Video S2). The electron transfer occurs when Tl(I) is already close to the three O_{2Mn} (2.30-2.38 Å), and coordinated to only two H_2O at a rather long distance (2.76-2.77 Å). The third H_2O is at 2.94 Å and moves in direction to Tl to complete its coordination to six (3O + 3W). The ω_2 frequency is low because weak bonds are involved in the $Tl^{1+}_{3O} \rightarrow Tl^{2+}_{3W,3O}$ reaction path. The energy barrier height of TS1 obtained by the frequency calculation is 3.0 kcal/mol.

The second electron transfer occurs when the three H_2O are at 2.44-2.47 Å from Tl(II). A second MnO_6 octahedron is elongated at the same time, undergoing a Jahn-Teller distortion characteristic of Mn(III) (Video S3). The TS2 vibrational transition mode has a frequency of ω_3 = -258 cm^{-1}, about 200 cm^{-1} higher than that of TS1, consistent with the formation of stronger (i.e., more covalent) Tl(III)-O bonds. The energy barrier height of TS2 is 3.8 kcal/mol. The complete energetic span model for the oxidation of Tl(I) to Tl(III) on basal planes is shown in Figure 4.

3.2.4. The Tl(I)-O_2 Oxidation Pathway. To be examined now is whether Tl(I) can be oxidized by molecular oxygen ($^3O_2$) at the δ-MnO_2 surface. This hypothesis is inspired from the oxidation of $[Mn(H_2O)_6]^{2+}$ by O_2, in which Mn(II) loses two electrons to a peroxo ligand (O_2^{2-}) as it adds the O_2 molecule into its coordination shell.[56] Two geometries were modeled, one with O_2^{2-} bound in an edge-on fashion to Tl-TCS, yielding a five-fold coordination, and one with O_2^{2-} and a water molecule bound to Tl-TCS, yielding a six-fold coordination (Figure 5). The two geometries are stable with a Mulliken atomic spin density of ~0 for Tl ($5d^{10}6s^0$) and ~3 for all Mn atoms ($3d^34s^2$). The two oxygen atoms are linked to each other through a π bond in the edge-on complex. The Gibbs free energy changes for the two oxygenation reactions are :

$$Tl^{1+}(H2O)_2 + O_2 + Mn^{4+}_{18}V \rightarrow Tl^{3+}_{5O}Mn^{4+}_{18}V + 2H_2O + 2H^+, \Delta G = 62.3 \text{ kcal/mol} \quad \text{(reaction 8)}$$

$$Tl^{1+}(H2O)_2 + O_2 + Mn^{4+}_{18}V \rightarrow Tl^{3+}_{W,5O}Mn^{4+}_{18}V + H_2O + 2H^+, \Delta G = 76.2 \text{ kcal/mol} \quad \text{(reaction 9)}$$

The two reactions are thermodynamically unfavorable. Furthermore, the Tl-peroxo distance is 2.14 Å, on average, and therefore incompatible with the Tl-H_2O EXAFS distance of 2.29 Å for the Tl(III)-TCS complex.[8]

3.3. Tl(I) Oxidation on Layer Edge Sites. The MnO_2 nanolayer used to model the oxidation of the Tl-DES complex counts 16 Mn(IV) octahedra and has no layer vacancy (Mn_{16}^{4+}, Figure 3b). The composition is $Mn_{16}O_{47}H_{28}$, its electronic charge is -2, and its spin multiplicity is M = 2S + 1 = 49. Tl forms a stable five-coordinated double-corner sharing (DCS) Tl(II) complex with a surface Mn(III) octahedron on layer edges ($Tl_{3W,2OH}^{2+}$, Figure 6a). The ΔG of formation of $Tl_{3W,2OH}^{2+}$ from Tl_{3W}^{1+} is 21.6 kcal/mol (reaction 10). The $Tl_{3W,2OH}^{2+}$ intermediate complex transforms into a Tl(III)-DES complex ($Tl_{3W,2OH,O}^{3+}$) with formation of a second Mn(III) octahedron when the OH_{2Mn} surface group is deprotonated (ΔG(reaction 11) = -4..4 kcal/mol, Figure 6b). Although the Tl(II) → Tl(III) reaction step is spontaneous, the $Tl_{3W,2OH,O}^{3+}$ product is 17.2 kcal/mol higher in energy than the Tl(I) reactant, and therefore the Tl(I) → Tl(III) oxidation pathway is endergonic without hydrolysis. The ΔG and pK_a of acid dissociation of the Tl(III)-DES complex are

$$Tl_{3W,2OH,O}^{3+} \rightarrow Tl_{2W,3OH,O}^{3+} + H^+,\ \Delta G = 0.5 \text{ kcal/mol},\ pK_4 = 0.4 \text{ (reaction 12)}$$

$$Tl_{2W,3OH,O}^{3+} \rightarrow Tl_{1W,4OH,O}^{3+} + H^+,\ \Delta G = 19.6 \text{ kcal/mol},\ pK_5 = 14.4 \text{ (reaction 13)}$$

$$Tl_{1W,4OH,O}^{3+} \rightarrow Tl_{5OH,O}^{3+} + H^+,\ \Delta G = 19.2 \text{ kcal/mol},\ pK_6 = 14.1 \text{ (reaction 14)}$$

The Gibbs free energy of formation of the monohydroxylated surface complex from aqueous Tl(I) is 17.2 + 0.5 = 17.7 kcal/mol. Because two protons are now released, one from the sorbent surface (OH_{2Mn} group) and one from the water molecule of the sorbate, this oxidation pathway is thermodynamically favorable at pH > 7 ($[Tl_{2W,3OH,O}^{3+}]/[Tl_{3W}^{1+}] > 1$). Taking ΔG = 17.7 – 4.5 = 13.2 kcal/mol yields pH > 4.9, when accounting for the systematic DFT error mentioned previously.

The weak interaction of Tl(I) with mineral surfaces poses a challenge for searching the TS of the Tl(I) → Tl(II) oxidation on layer edges. For this attempt, one needs to guesstimate how the Tl^{1+} ion approaches the protonated oxygen atoms of the Mn(IV) octahedra at the layer surface and this requires some intuition to make educated choices. There is clearly no unequivocal structure model for the Tl(I) surface complex. Explicit solvent molecular dynamics simulations, which are beyond the scope of this article, might be more adapted to investigate this step.

4. CONCLUDING REMARKS

In this study, we set out to model the oxidation of Tl(I) by Mn(IV) on basal planes and layer edges of birnessite (δ-MnO_2). The main picture which emerges from this study is that the standard change in

free energy of the oxidative uptake of Tl(I) by birnessite is positive, and therefore non-spontaneous unless a supplementary driving force is provided. At pH higher than 4-5, additional energy is yielded by the hydrolysis of the product, which is an exergonic reaction. The experimentally observed pH-dependence of the oxidation reaction[3,4] is in full agreement with our current findings. The Tl oxidation free energies fundamentally contrast with the oxidation energies of Co(II) to Co(III) by birnessite, in which the product is 17.6 kcal/mol more stable than the reactant and not hydrolyzed.[33] The week oxidizability of Tl(I) explains its co-occurrence with Tl(III) in marine ferromanganese deposits[8] and laboratory studies. [2–4] Tl(I) interacts weekly with hydroxyl groups at the mineral surface, for it is also little hydrolyzable. As such, it is unable to substitute for Mn^{3+}_{TCS}-Mn^{3+}_{Layer} pair-forming interlayer Mn(III), in contrast to Co(II). Thus, the oxidative uptake of Tl(I) occurs on unblocked vacancy sites, as suggested by Wick et al.[2]

Another highlight of this study is the identification of an intermediate Tl(II) state on the two surface sites, which participates in two energy-equivalent reactions proceeding by one-electron-transfer steps. This electronic process may be observationally indistinguishable from a single two-electron step given the highly reactive nature of the intermediate oxidation state which participates in redox reactions with one-electron-transfer steps. This issue has been addressed previously by George Luther regarding the oxidation of Mn(II) to Mn(IV) in the environment.[56]

Tl(I) to Tl(III) oxidation in two successive one-electron steps may produce two Mn(III) or a single Mn(II) if the two electrons are transferred to the same Mn atom. DFT supports the first process as no Mn atom had a spin density close to 5. At first glance, this result seems at variance with the measurement of Mn(II) in solution at pH 4 where little re-adsorption to the δ-MnO_2 surface occurs.[4] This experiment was performed at high Tl/Mn ratio, and therefore may have produced an excess Mn(III), which is known to disproportionate to Mn(IV) and Mn(II), as observed in the transformation of monoclinic/triclinic birnessite to hexagonal birnessite at acidic pH.[24,25]

ASSOCIATED CONTENT

Supporting Information

Electronic charge and multiplicity of the structure models and spin density of Tl (PDF)

(Video S1) Formation of a H-bond between an H_2O molecule coordinated to Tl(I) and a layer O_{3Mn} surface oxygen (ω_1 = -78 cm^{-1} calculated at the PBE0/tzvp-D3B level) (AVI)

(Video S2) Formation of the three Tl-H_2O bonds during the $Tl^{1+}_{3O} \rightarrow Tl^{2+}_{3W,3O}$ reaction path (ω_1 = -65 cm^{-1} calculated at the PBE0/tzvp-D3B level) (AVI)

(Video S3) Shortening of the Tl-H_2O bond lengths and Jahn-Teller distorsion of a Mn octahedron during the $Tl^{2+}_{3W,3O} \rightarrow Tl^{3+}_{3W,3O}$ reaction path (ω_3 = -258 cm^{-1} calculated at the PBE0/tzvp-D3B level) (AVI)

AUTHOR INFORMATION

Corresponding Author

E-mail: alain.manceau@ens-lyon.fr

ORCID

Alain Manceau: 0000-0003-0845-611X

Stephan N. Steinmann: 0000-0002-2777-356X

Notes

The authors declare no competing financial interests.

ACKNOWLEDGEMENTS

The GRICAD laboratory from the University Grenoble Alpes provided computing resources. Financial support was provided by the European Research Council under Advanced Grant DEEP-SEE (#101052913). Two anonymous reviewers are acknowledged for constructive comments on the manuscript.

REFERENCES

(1) Peacock, C. L.; Moon, E. M. Oxidative Scavenging of Thallium by Birnessite: Explanation for Thallium Enrichment and Stable Isotope Fractionation in Marine Ferromanganese Precipitates. *Geochim. Cosmochim. Acta* **2012**, *84*, 297–313.

(2) Wick, S.; Pena, J.; Voegelin, A. Thallium Sorption onto Manganese Oxides. *Environ. Sci. Technol.* **2019**, *53*, 13168–13178.

(3) Ruiz-Garcia, M.; Villalobos, M.; Voegelin, A.; Pi-Puig, T.; Nadia Martínez-Villegas; Göttlicher, J. Transformation of Hexagonal Birnessite upon Reaction with Thallium(I): Effects of Birnessite Crystallinity, pH, and Thallium Concentration. *Env. Sci. Technol.* **2021**, *55*, 4862–4870.

(4) Cruz-Hernandez, Y.; Villalobos, M.; Marcus, M. A.; Pi-Puig, T.; Zanella, R.; Martinez-Villegas, N. Tl(I) Sorption Behavior on Birnessite and Its Implications for Mineral Structural Changes. *Geochim. Cosmochim. Acta* **2019**, *248*, 356–369.

(5) Aguilar-Carrillo, J.; Herrera-Garcia, L.; Reyes-Dominguez, I. A.; Gutierrez, E. J. Thallium(I) Sequestration by Jarosite and Birnessite: Structural Incorporation vs Surface Adsorption. *Environ. Pollut.* **2020**, *257*, n° 113492.

(6) Zou, Y.; Cheng, H.; Wang, H.; Huang, R.; Xu, Y.; Jiang, J.; He, Q.; Liu, C.; Liu, J.; Xiong, J.; Yao, J.; Huangfu, X.; Ma, J. Thallium(I) Oxidation by Permanganate and Chlorine: Kinetics and Manganese Dioxide Catalysis. *Environ. Sci. Technol.* **2020**, *54*, 7205–7216.

(7) Marafatto, F. F.; Dähn, R.; Grolimund, D.; Göttlicher, J.; Voegelin, A. Thallium Sorption by Soil Manganese Oxides: Insights from Synchrotron X-Ray Micro-Analyses on a Naturally Thallium-Rich Soil. *Geochim. Cosmochim. Acta* **2021**, *302*, 193–208.

(8) Manceau, A.; Simionovici, A.; Findling, N.; Glatzel, P.; Detlefs, B.; Wegorzewski, A. V.; Mizell, K.; Hein, J. R.; Koschinsky, A. Crystal Chemistry of Thallium in Marine Ferromanganese Deposits. *ACS Earth & Space Chem.* **2022**, *6*, 1269–1285.

(9) Wick, S.; Baeyens, B.; Fernandes, M. M.; Voegelin, A. Thallium Adsorption onto Illite. *Environ. Sci. Technol.* **2018**, *52*, 571–580.

(10) Xu, H.; Luo, Y.; Wang, P.; Zhu, J.; Yang, Z.; Liu, Z. Removal of Thallium in Water/Wastewater: A Review. *Water Res.* **2019**, *165*.

(11) Voegelin, A.; Pfenninger, N.; Petrikis, J.; Majzlan, J.; Plotze, M.; Senn, A. C.; Mangold, S.; Steininger, R.; Gottlicher, J. Thallium Speciation and Extractability in a Thallium- and Arsenic-Rich Soil Developed from Mineralized Carbonate Rock. *Environ. Sci. Technol.* **2015**, *49*, 5390–5398.

(12) Wick, S.; Baeyens, B.; Fernandes, M. M.; Gottlicher, J.; Fischer, M.; Pfenninger, N.; Plotze, M.; Voegelin, A. Thallium Sorption and Speciation in Soils: Role of Micaceous Clay Minerals and Manganese Oxides. *Geochim. Cosmichim. Acta* **2020**, *288*, 83–100.

(13) Zhuang, W.; Liu, M.; Song, J. M.; Ying, S. C. Retention of Thallium by Natural Minerals: A Review. *Sci. Tot. Environ.* **2021**.

(14) Huangfu, X. L.; Jiang, J.; Lu, X. X.; Wang, Y.; Liu, Y. Z.; Pang, S. Y.; Cheng, H. J.; Zhang, X.; Ma, J. Adsorption and Oxidation of Thallium(I) by a Nanosized Manganese Dioxide. *Wat. Air Soil Pollut.* **2015**, *226*.

(15) Huangfu, X. L.; Ma, C. X.; Ma, J.; He, Q.; Yang, C.; Zhou, J.; Jiang, J.; Wang, Y. A. Effective Removal of Trace Thallium from Surface Water by Nanosized Manganese Dioxide Enhanced Quartz Sand Filtration. *Chemosphere* **2017**, *189*, 1–9.

(16) Zhang, L.; Yang, Y.; Xu, X.; Deng, S.; Xiao, H.; Han, X.; Xia, F.; Jiang, Y. Efficient Utilization of Biogenic Manganese Oxides in Bioaugmentation Columns for Remediation of Thallium(I) Contaminated Groundwater. *J. Hazard. Mater.* **2023**, in press.

(17) Lennartson, A. Toxic Thallium. *Nature Chem.* **2015**, *7*, 610–610.

(18) Cruz-Hernandez, Y.; Ruiz-Garcia, M.; Villalobos, M.; Romero, F.; Meza-Figueroa, D.; Garrido, F.; Hernandez-Alvarez, E.; Pi-Puig, T. Fractionation and Mobility of Thallium in Areas Impacted by Mining-Metallurgical Activities: Identification of a Water-Soluble Tl(I) Fraction. *Environ. Pollut.* **2018**, *237*, 154–165.

(19) Dordevic, T.; Karasalihovic, T.; Stöge-Pollach, M.; Karanovic, L. Tl(I) Sequestration by Pharmacosiderite Supergroup Arsenates: Synthesis, Crystal Structures and Relationships in Tl(I)–M(III)–As(V)–H2O (M = Al, Fe) System. *Mineral. Petrol.* **2023**, *117*, in press.

(20) Hein, J. R.; Koschinsky, A. Deep-Ocean Ferromanganese Crusts and Nodules. In *Treatrise on Geochemistry*; Holland, H. D., Turekian, K. K., Eds.; Oxford: Elsevier, 2014; Vol. 1–16, pp 273-291.

(21) Casiot, C.; Egal, M.; Bruneel, O.; Verma, N.; Parmentier, M.; Elbaz-Poulichet, F. Predominance of Aqueous Tl(I) Species in the River System Downstream from the Abandoned Carnoules Mine (Southern France). *Environ. Sci. Technol.* **2011**, *45*, 2056–2064.

(22) Nriagu, J. O. *Thallium in the Environment.*; John Wiley & Sons, Inc.,: New York, 1998.

(23) Bidoglio, G.; Gibson, P. N.; O'Gorman, M.; Roberts, K. J. X-Ray Absorption Spectroscopy Investigation of Surface Redox Transformations of Thallium and Chromium on Colloidal Mineral Oxides. *Geochim. Cosmochim. Acta* **1993**, *57*, 2389–2394.

(24) Drits, V. A.; Silvester, E.; Gorshkov, A. I.; Manceau, A. Structure of Synthetic Monoclinic Na-Rich Birnessite and Hexagonal Birnessite. Part 1. Results from X-Ray Diffraction and Selected Area Electron Diffraction. *Am. Miner.* **1997**, *82*, 946–961.

(25) Silvester, E.; Manceau, A.; Drits, V. Structure of Synthetic Monoclinic Na-Rich Birnessite and Hexagonal Birnessite .2. Results from Chemical Studies and EXAFS Spectroscopy. *Am. Miner.* **1997**, *82*, 962–978.

(26) Lanson, B.; Drits, V. A.; Silvester, E. J.; Manceau, A. Structure of H-Exchanged Hexagonal Birnessite and Its Mechanism of Formation from Na-Rich Monoclinic Buserite at Low PH: New Data from X-Ray Diffraction. *Am. Miner.* **2000**, *85*, 826–835.

(27) Lanson, B.; Drits, V. A.; Feng, Q.; Manceau, A. Structure of Synthetic Na-Birnessite: Evidence for a Triclinic One-Layer Unit Cell. *Am. Miner.* **2002**, *87*, 1662–1671.

(28) Manceau, A.; Marcus, M. A.; Grangeon, S.; Lanson, M.; Lanson, B.; Gaillot, A. C.; Skanthakumar, S.; Soderholm, L. Short-Range and Long-Range Order of Phyllomanganate Nanoparticles Determined Using High Energy X-Ray Scattering. *J. Appl. Crystallogr.* **2013**, *46*, 193–209.

(29) Gaillot, A. C.; Flot, D.; Drits, V. A.; Burghammer, M.; Manceau, A.; Lanson, B. Structure of Synthetic K-Rich Birnessites Obtained by High-Temperature Decomposition of $KMnO_4$. I. Two-Layer Polytype from a 800°C Experiment. *Chem. Mater.* **2003**, *15*, 4666–4678.

(30) Villalobos, M.; Lanson, B.; Manceau, A.; Toner, B.; Sposito, G. Structural Model for the Biogenic Mn Oxide Produced by *Pseudomonas Putida*. *Am. Miner.* **2006**, *91*, 489–502.

(31) Manceau, A.; Kersten, M.; Marcus, M. A.; Geoffroy, N.; Granina, L. Ba and Ni Speciation in a Nodule of Binary Mn Oxide Phase Composition from Lake Baikal. *Geochim. Cosmochim. Acta.* **2007**, *71*, 1967–1981.

(32) Gaillot, A. C.; Drits, V. A.; Manceau, A.; Lanson, B. Structure of the Synthetic K-Rich Phyllomanganate Birnessite Obtained by High-Temperature Decomposition of $KMnO_4$: Substructures of K-Rich Birnessite from 1000°C Experiment. *Micropor. Mesopor. Mat.* **2007**, *98*, 267–282.

(33) Manceau, A.; Steinmann, S. N. Density Functional Theory Modeling of the Oxidation Mechanism of Co(II) by Birnessite. *ACS Earth Space Chem.* **2022**, *6*, 2063–2075.

(34) Manceau, A.; Drits, V. A.; Silvester, E.; Bartoli, C.; Lanson, B. Structural Mechanism of Co(II) Oxidation by the Phyllomanganate, Na-Buserite. *Am. Miner.* **1997**, *82*, 1150–1175.

(35) Simanova, A. A.; Peña, J. Time-Resolved Investigation of Cobalt Oxidation by Mn(III)-Rich δ-MnO_2 Using Quick X-Ray Absorption Spectroscopy. *Environ. Sci. Technol.* **2015**, *18*, 10867–10876.

(36) Lin, T.; Nriagu, J. Revised Hydrolysis Constants for Thallium(I) and Thallium(III) and the Environmental Implications. *J. Air Waste Manag. Assoc.* **1998**, *48*, 151–156.

(37) Neese, F.; Wennmohs, F.; Becker, U.; Riplinger, C. The ORCA Quantum Chemistry Program Package. *J. Chem. Phys.* **2020**, *152*, n° 224108.

(38) Manceau, A.; Steinmann, S. N. Nature of High- and Low-Affinity Metal Surface Sites on Birnessite Nanosheets. *ACS Earth Space Chem.* **2021**, *5*, 66–76.

(39) Colinet, P.; Gheeraert, A.; Curutchet, A.; Le Bahers, T. On the Spectroscopic Modeling of Localized Defects in Sodalites by TD-DFT. *J. Phys. Chem C* **2020**, *124*, 8949–8957.

(40) Adamo, C.; Barone, V. Toward Reliable Density Functional Methods without Adjustable Parameters: The PBE0 Model. *J. Chem. Phys.* **1999**, *110*, 6158–6170.

(41) Perdew, J. P.; Ernzerhof, M. Rationale for Mixing Exact Exchange with Density Functional Approximations. *J. Chem. Phys.* **1996**, *105*, 9982–9985.

(42) Grimme, S.; Ehrlich, S.; Goerigk, L. Effect of the Damping Function in Dispersion Corrected Density Functional Theory. *J. Comput. Chem.* **2011**, *32*, 1456–1465.

(43) Weigend, F.; Ahlrichs, R. Balanced Basis Sets of Split Valence, Triple Zeta Valence and Quadruple Zeta Valence Quality for H to Rn: Design and Assessment of Accuracy. *Phys. Chem. Chem. Phys.* **2005**, *7*, 3297–3305.

(44) Metz, B.; Schweizer, M.; Stoll, H.; Dolg, M.; Liu, W. A Small-Core Multiconfiguration Dirac-Hartree-Fock-Adjusted Pseudopotential for Tl-Application to TlX (X = F, Cl, Br, I). *Theor. Chem. Acc.* **2000**, *104* (1), 22–28.

(45) Weigend, F. Accurate Coulomb-Fitting Basis Sets for H to Rn. *Phys. Chem. Chem. Phys.* **2006**, *8*, 1057–1065.

(46) Besora, M.; Vidossich, P.; Lledos, A.; Ujaque, G.; Maseras, F. Calculation of Reaction Free Energies in Solution: A Comparison of Current Approaches. *J. Phys. Chem. A* **2018**, *122*, 1392–1399.

(47) Marenich, A. V.; Cramer, C. J.; Truhlar, D. G. Universal Solvation Model Based on Solute Electron Density and on a Continuum Model of the Solvent Defined by the Bulk Dielectric Constant and Atomic Surface Tensions. *J. Phys. Chem. B* **2009**, *113*, 6378–6396.

(48) Kelly, C. P.; Cramer, C. J.; Truhlar, D. G. Aqueous Solvation Free Energies of Ions and Ion-Water Clusters Based on an Accurate Value for the Absolute Aqueous Solvation Free Energy of the Proton. *J. Phys. Chem. B.* **2006**, *110*, 16066–16081.

(49) Harvey, J.; Aschi, M.; Schwarz, H.; Koch, W. The Singlet and Triplet States of Phenyl Cation. A Hybrid Approach for Locating Minimum Energy Crossing Points between Non-Interacting Potential Energy Surfaces. *Theor. Chem. Acc.* **1998**, *99*, 95–99.

(50) Smith, R. M.; Martell, A. E.; Motekaitis, R. J. *NIST Critically Selected Stability Constants of Metal Complexes Database. NIST Standard Reference Database 46, Version 7.0*; NIST, Gaithersburg, MD, USA, 2003.

(51) Persson, I.; Jalilehvand, F.; Sandstrom, M. Structure of the Solvated Thallium(I) Ion in Aqueous, Dimethyl Sulfoxide, N,N ’-Dimethylpropyleneurea, and N,N-Dimethylthioformamide Solution. *Inorg. Chem.* **2002**, *41*, 192–197.

(52) Reed, A. E.; Weinstock, R. B.; Weinhold, F. Natural-Population Analysis. *J. Chem. Phys.* **1985**, *83*, 735–746.

(53) Reed, A. E.; Curtiss, L. A.; Weinhold, F. Intermolecular Interactions from a Natural Bond Orbital, Donor-Acceptor Viewpoint. *Chem. Rev.* **1988**, *88*, 899–926.

(54) Glendening, E. D.; Landis, C. R.; Weinhold, F. NBO 6.0: Natural Bond Orbital Analysis Program. *J. Comput. Chem.* **2013**, *34*, 1429–1437.

(55) Asgeirsson, V.; Birgisson, B. O.; Bjornsson, R.; Becker, U.; Neese, F.; Riplinger, C.; Jonsson, H. Nudged Elastic Band Method for Molecular Reactions Using Energy-Weighted Springs Combined with Eigenvector Following. *J. Chem. Theory Comput.* **2021**, *17*, 4929–4945.

(56) Luther, G. W. Manganese(II) Oxidation and Mn(IV) Reduction in the Environment - Two One-Electron Transfer Steps versus a Single Two-Electron Step. *Geomicrobiol. J.* **2005**, *22*, 195–203.

Figure Caption

Figure 1. Polyhedral representation of a Mn(IV) vacancy site (a), a TCS complex (b), and a DES complex (c).

Figure 2. Schematic pathways of reactions 1-4 on vacancy sites. (a) In reaction 1, solvated Tl(I) forms a monodentate complex with the O_{2Mn} oxygen bordering a vacancy. (b) In reaction 2, Tl(I) forms a dehydrated TCS complex. (c) In reaction 3, the Tl(I)-TCS complex is oxidized to an octahedral Tl(II)-TCS complex by an adjacent layer Mn(IV), which is reduced to Mn(III). In reaction 4, the Tl(II) is oxidized to Tl(III) by a second Mn(IV).

Figure 3. NEB-optimized energy profiles along the Tl(I) → Tl(II) (a), and the Tl(II) → Tl(III) reaction coordinates (b).

Figure 4. Energetic span model of the oxidation of Tl(I) to Tl(III) on deprotonated Mn(IV) vacancy sites in birnessite.

Figure 5. Polyhedral representation of the oxygenated Tl(III) complexes over a vacancy site. (a) Five-coordinated edge-on complex. (b) Six-coordinated Tl(III) complex.

Figure 6. Schematic pathways of reactions 10 and 11 on edge sites. (a) In reaction 11, solvated Tl(I) is oxidized to a bidentate Tl(II)-DCS complex by an adjacent Mn(IV), which is reduced to Mn(III). In reaction 11, the Tl(II)-DCS complex is oxidized to a Tl(III)-DES complex by a second Mn(IV).

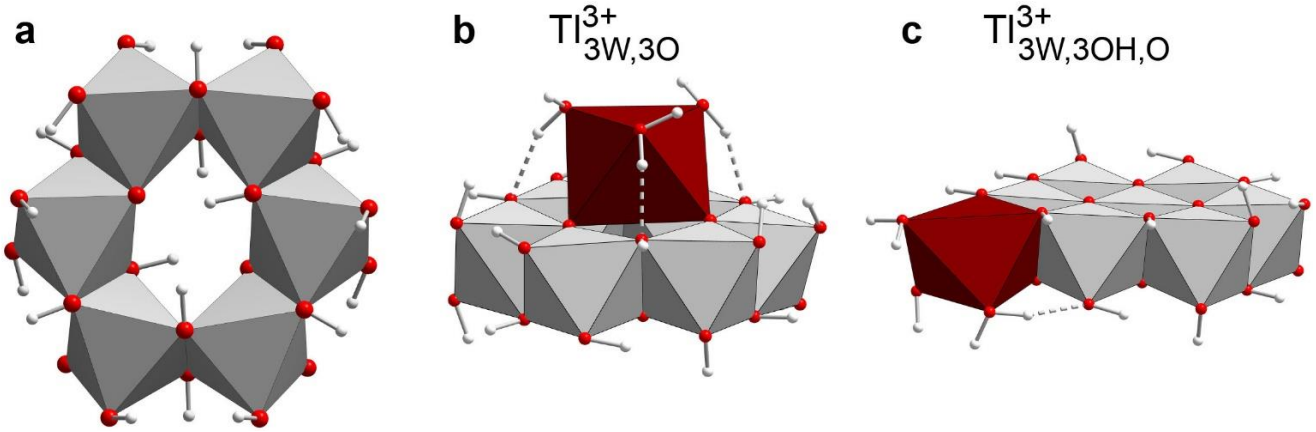

Figure 1

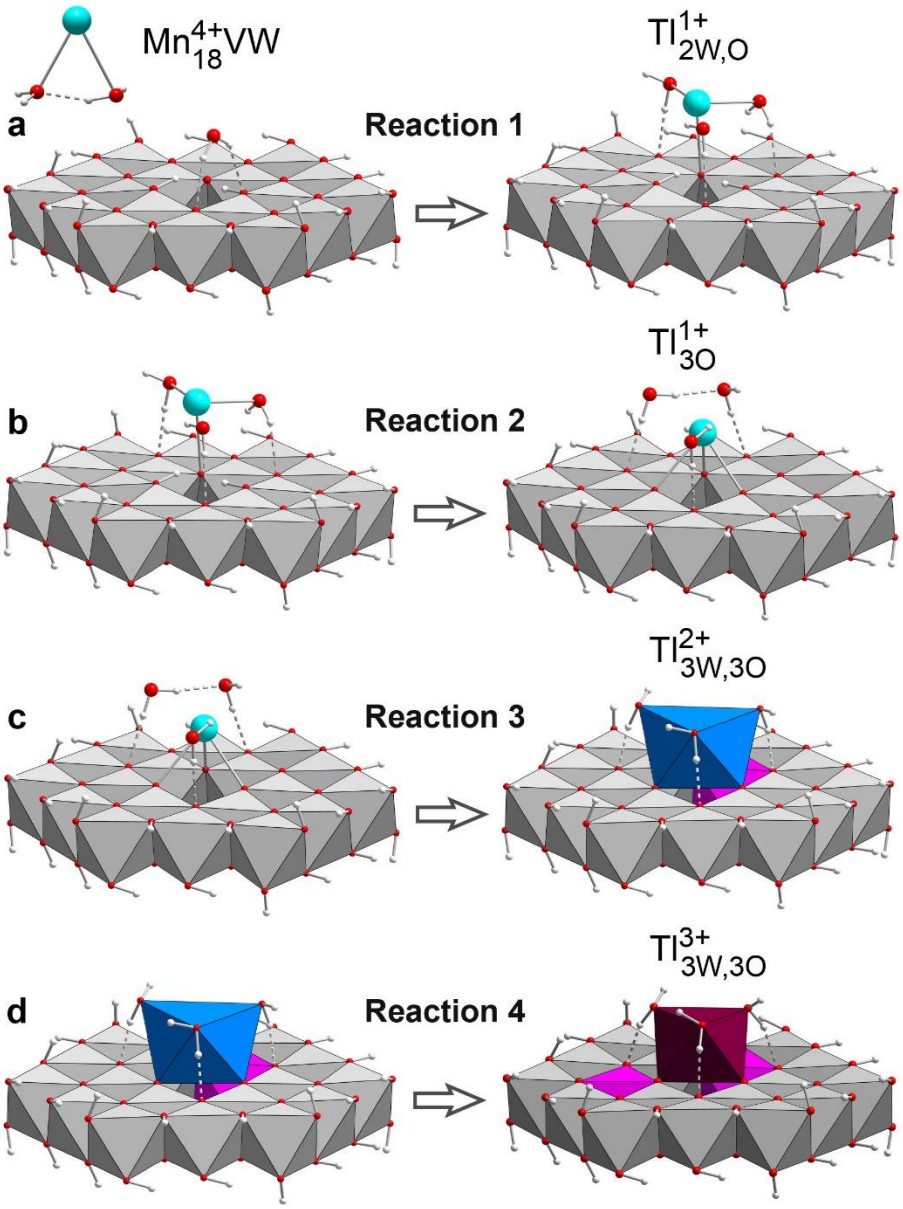
$Mn_{18}^{4+}VW$
$Tl_{2W,O}^{1+}$
a
Reaction 1
Tl_{3O}^{1+}
b
Reaction 2
$Tl_{3W,3O}^{2+}$
c
Reaction 3
$Tl_{3W,3O}^{3+}$
d
Reaction 4

Figure 2

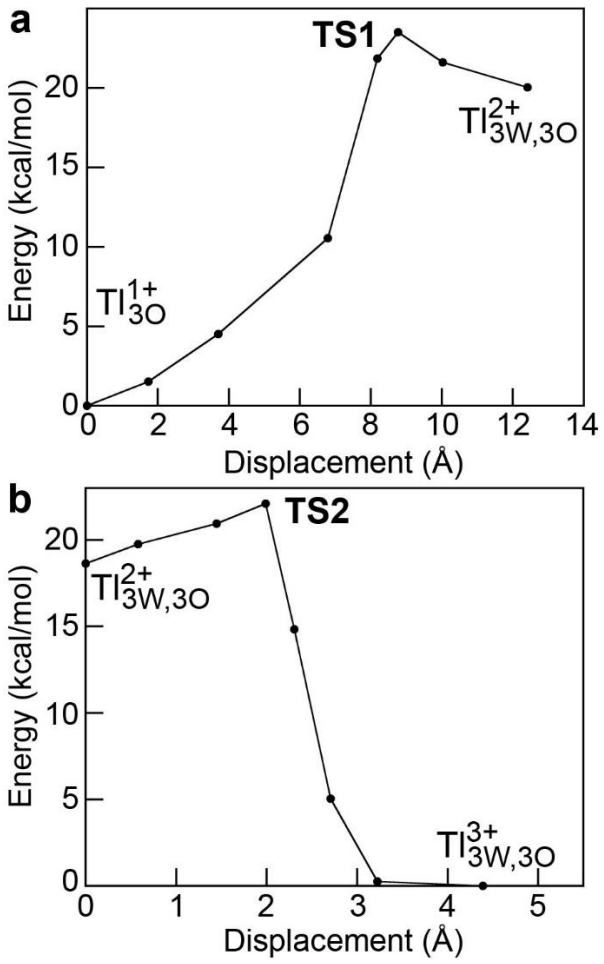
a
TS1
$Tl^{2+}_{3W,3O}$
Tl^{1+}_{3O}
Energy (kcal/mol)
Displacement (Å)
b
TS2
$Tl^{2+}_{3W,3O}$
$Tl^{3+}_{3W,3O}$
Energy (kcal/mol)
Displacement (Å)

Figure 3

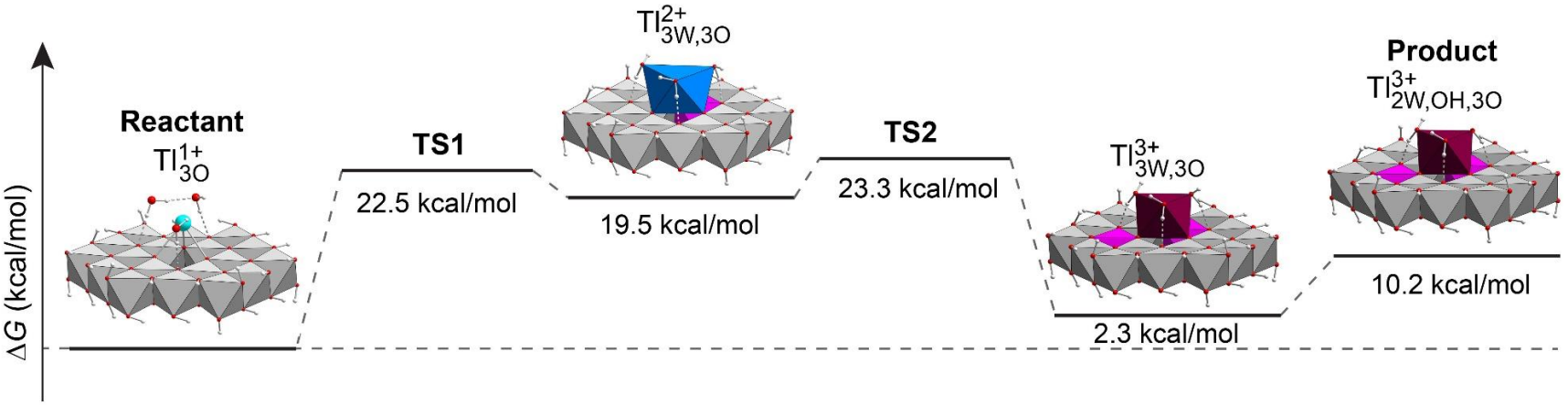
ΔG (kcal/mol)
Reactant
Tl^{1+}_{3O}
TS1
22.5 kcal/mol
$Tl^{2+}_{3W,3O}$
19.5 kcal/mol
TS2
23.3 kcal/mol
$Tl^{3+}_{3W,3O}$
2.3 kcal/mol
Product
$Tl^{3+}_{2W,OH,3O}$
10.2 kcal/mol

Figure 4

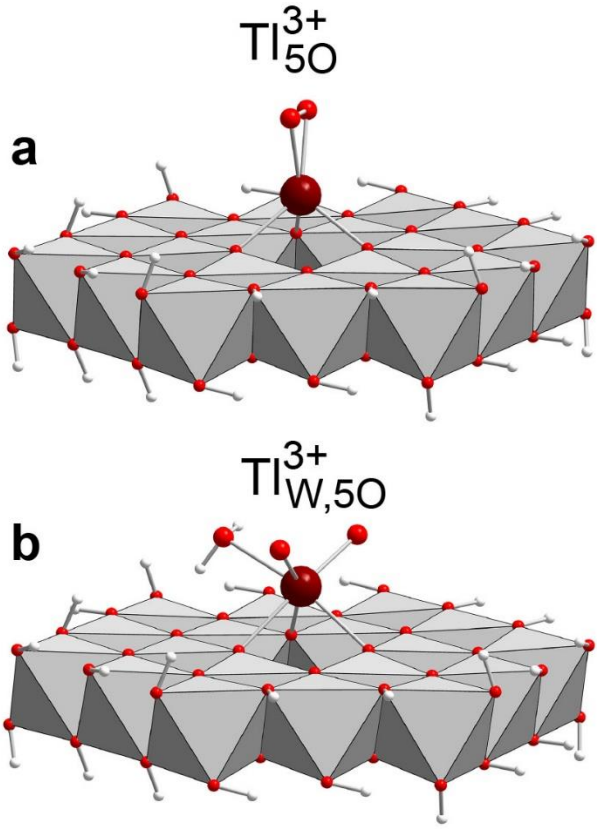

Figure 5

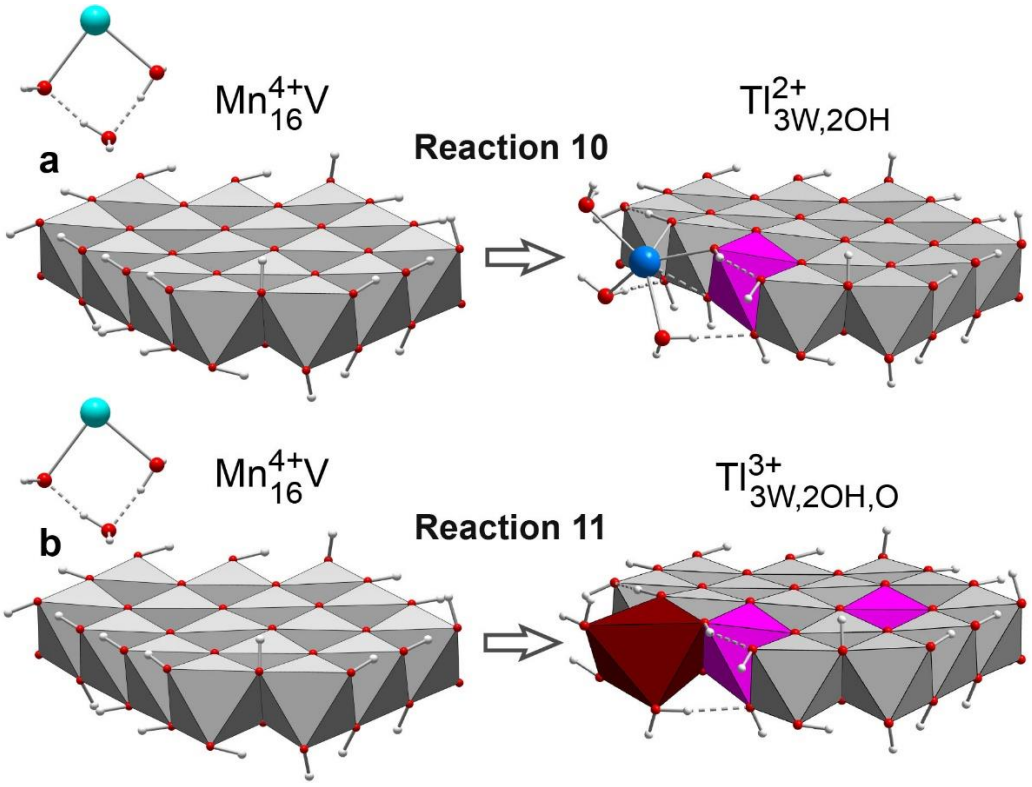
a
$Mn_{16}^{4+}V$
Reaction 10
$Tl_{3W,2OH}^{2+}$
b
$Mn_{16}^{4+}V$
Reaction 11
$Tl_{3W,2OH,O}^{3+}$

Figure 6

Supplementary Information

Density Functional Theory Modeling of the Oxidation Mechanism of Tl(I) by Birnessite

Alain Manceau[*a,b] and Stephan N. Steinmann[a]

[a] ENS de Lyon, CNRS, Laboratoire de Chimie, F-69342 Lyon, France

[b] European Synchrotron Radiation Facility (ESRF), F-38000 Grenoble, France

Supplementary Table

Table S1. Total electronic charge, Mulliken atomic spin density (ρ), and multiplicity of the structure models

Basal complexes	Charge	Spin density Tl	Multiplicity
$Mn_{18}^{4+}VW$	-2	-	55
$Tl_{2W,O}^{1+}$	-1	0.00	55
Tl_{3O}^{1+}	-3	0.01	55
$Tl_{3W,3O}^{2+}$	-3	-0.06	55
$Tl_{3W,3O}^{3+}$	-3	0.03	57
Tl_{5O}^{3+}	-3	0.03	55
$Tl_{W,5O}^{3+}$	-3	0.02	55
Edge complexes			
$Mn_{16}^{4+}V$	-2	-	49
$Tl_{3W,2OH,O}^{3+}$	-2	0.03	51
$Tl_{3W,2OH}^{2+}$	-1	0.65	51

Supplementary Figure

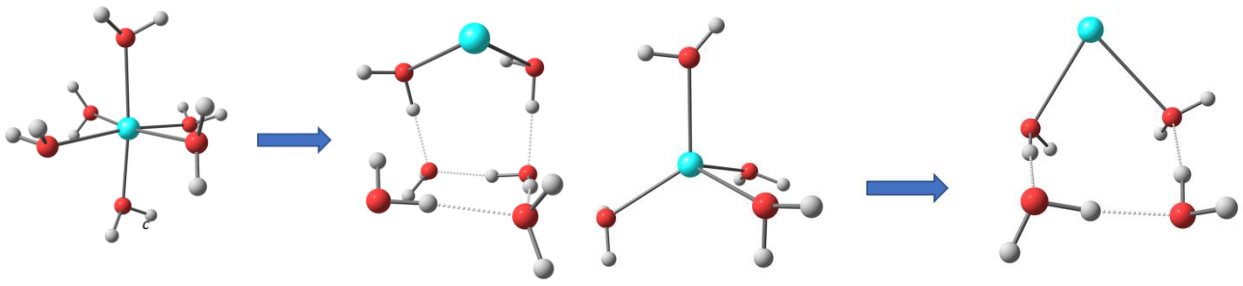

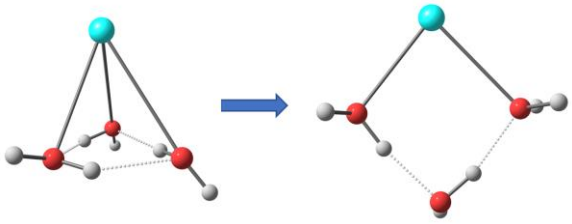

Fig. S1. Geometry optimization of a six-, four-, and three-fold coordination of Tl(I) with water molecules, showing that the two-fold coordination is the stable structure in solution.

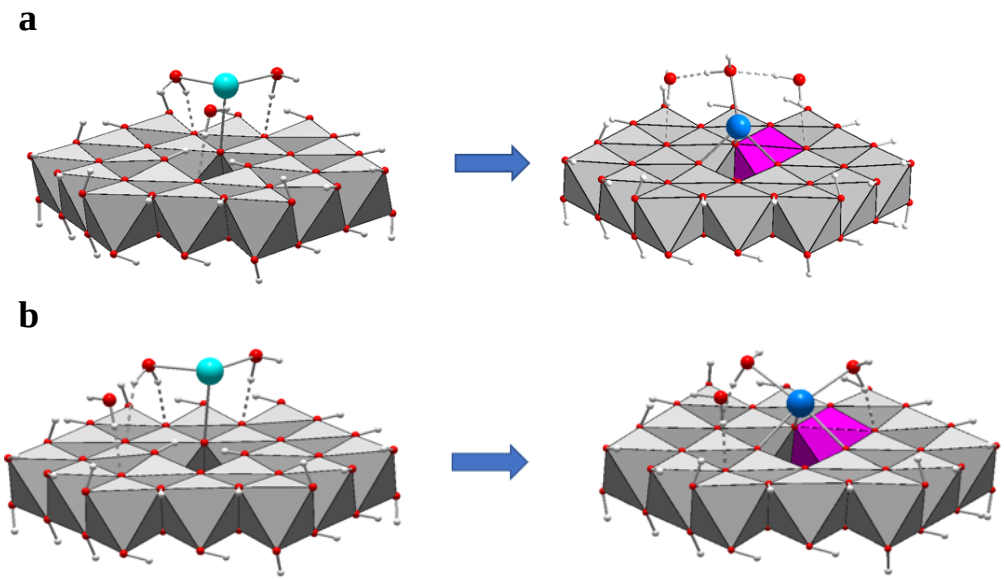

Fig. S2. Oxidation of Tl(I) to Tl(II) with formation of a four-fold $Tl^{2+}_{W,3O}$ complex (a) and a five-fold $Tl^{2+}_{2W,3O}$ complex (b). The Gibbs free energy of formation of the $Tl^{2+}_{W,3O}$ complex is ΔG = 24.6 kcal/mol and that of the $Tl^{2+}_{2W,3O}$ complex is ΔG = 23.9 kcal/mol.